Please cite the Published Version

Data Access Statement: Data will be made available on request.

Enhancing NO$_2$ sensing performance through interface engineering in Cs$_2$AgBiBr$_6$/SnO$_2$/ZnO-NRs sensor

Shifeng Wang[a#], Hui Hu[a#], Tian Tan[a], Xun Li[a], Wanlin Zhou[a], Zhanyou Tian[a], Yuwen Bao[a], K. P. Homewood[a], Sohail Muhammad[b*], Xiaohong Xia[a,*], and Yun Gao[a,*]

[a] Ministry-of-Education Key Laboratory for the Green Preparation and Application of Functional Materials, School of Materials Science & Engineering, Hubei University, Wuhan 430062, China.

[b] Department of Natural Sciences, Faculty of Science and Engineering, Manchester Metropolitan University, M15 6BH United Kingdom

[#]Shifeng Wang and Hui Hu have equal contributions to this work.

*Corresponding Authors:

Email addresses: Muhammad.sohail@mmu.ac.uk, xhxia@hubu.edu.cn; gaoyun@hubu.edu.cn.

Abstract

Developing sensors that operate under ambient conditions with minimal energy consumption, ensuring a robust response and efficient recovery to toxic NO$_2$ gas, can help take appropriate and corrective measures to protect human health from exposure to hazardous environments. In this study, we have successfully designed a gas sensor device based on a sandwoch structure of Cs$_2$AgBiBr$_6$/SnO$_2$/ZnO-nanorods (CABB/SnO$_2$/ZnO-NRs) for detecting NO$_2$ at room temperature. The insertion of the SnO$_2$ layer between the CABB and ZnO-NRs, which works as a hole blocker, not only improves significantly the sensor stability from a few hours to more than a month but

also offers the energy step for electron transfer from ZnO-NRs to CABB. The CABB layer further enhances the charge separation, transport, and conductivity from the perovskite to the ZnO surface, actively participating in the gas-sensitive reaction. The response of CABB/SnO$_2$/ZnO-NRs sensors to 100 ppm NO$_2$ is about 9 times higher than that of ZnO-NRs, showing a significantly improved NO$_2$ sensing performance.

1. **Introduction**

The release of toxic and harmful gases from technological and industrial developments inevitably impacts the natural environment and living organisms [1]. NO$_2$ gas is a critical indicator for the assessment of air quality. High concentrations of NO$_2$ in the atmosphere could result in the formation of acid rain and photochemical smog formation [2, 3]. Long-term exposure to NO$_2$ will significantly impact human health [4]. Extensive research has demonstrated that high levels of nitrogen dioxide pollution in urban areas contribute to two-thirds of asthma cases among children [5]. Short-term exposure to 50 ppm NO$_2$ may cause damage to the respiratory system [6]. Therefore, detecting NO$_2$ with low concentration detection limit is crucial from various perspectives.

Metal oxide semiconductor (MOS) gas sensors are widely used in environmental gas detection due to their low raw material cost, ease of preparation, high response and short response time [7]. Commonly used oxide semiconductor gas sensing materials

include ZnO, SnO$_2$, TiO$_2$ and NiO. However, these materials exhibit widespread shortcomings such as high operating temperature, long recovery time, poor stability, and limited selectivity [8-11]. To address these issues, various strategies such as element doping [12], formation of heterojunction [13], nanostructure [14], design morphology and structure [15] are implemented to enhance the sensors' performance. In recent years, there has been a growing interest in the utilization of perovskite materials in gas sensing applications, owing to their optoelectronic characteristics such as high carrier mobility, extended carrier lifetime, significant absorption coefficient and other advantages [16-18]. The flexible ABX$_3$ structure of the perovskite allows for precise tuning of optoelectronic properties to meet specific requirements for various applications, including sensors. A detailed examination of perovskite nanomaterials reveals alterations in optoelectronic properties when exposed to gases such as NO$_2$, CH$_4$, NH$_3$, C$_2$H$_5$OH, making them suitable for gas sensing applications [19-21]. Property changes can be detected by recording the variations in electrical resistance, phosphorescence, or fluorescence response, etc., to monitor the concentration of gases in the environment [22-24]. Fu et al. utilized a spin coating method to prepare an organic and inorganic hybrid perovskite p-type CH$_3$NH$_3$PbI$_3$ film, demonstrating rapid sensing of NO$_2$ at room temperature, and elucidating the chemical adsorption induced gas-sensitive mechanism by in-situ FTIR [25]. Kim et al. fabricated inorganic CsPbBr$_3$ perovskite thin-film using hot injection followed by soft soaking treatment to enhance carrier life and selectivity for NO$_2$ [26]. However, single perovskite films as gas sensing layers show characteristics such as long response times, low sensitivity and insufficient

stability. Li et al. found that ZnO micro balls (MBs) decorated with $CsPbBr_3$ quantum dots (QDs) showed an improved NO_2 sensing performance with high response and stability under light illumination, but poor humidity resistance to NO_2 [27]. Ye et al. demonstrated that halide perovskite Cs_2PbBr_6 linked with two-dimensional covalent organic frameworks (2D COF) can significantly enhance the selectivity and sensitivity to NO_2 [28]. Nevertheless, perovskites containing lead pose environment and human health risks, potentially hindering their large-scale application in gas sensors. To develop lead-free perovskites with high stability is a crucial concern for real applications, and the relevant mechanism concerning the stability requires a deep understanding.

In this study, we used lead-free double perovskite $Cs_2AgBiBr_6$ (CABB) film in conjunction a with a ZnO-nanorods (ZnO-NRs) array to enhance the device's response to NO_2 gas. Further optimization of the sensing device involved interface engineering through addition of a SnO_2 layer between the two films. The experimental results indicate that the presence of a SnO_2 layer between the zinc oxide and perovskite layers provides special energy band alignment, improves gas responsiveness and enhances sensing stability compared to the films without the layer, demonstrating fast response and recovery properties.

2. Experimental section

2.1. Synthesis of ZnO-NRs film

Initially, a dense and uniform seed layer of ZnO nanoparticles was applied on a glass substrate using the spin coating method, followed by annealing as detailed in a previous

report [29]. Subsequently, ZnO nanorods (ZnO-NRs) were grown on the ZnO seed layer using the hydrothermal method. The glass, coated with the ZnO seed layer, was positioned diagonally with the seed layer facing downward immersed into a 200 mL Teflon−lined autoclave containing 0.05 M of $Zn(NO_3)_2 \cdot 6H_2O$ and 0.05 M hexamethylenetetramine (HMTA). The hydrothermal reaction took place at 90°C for 8h. Finally, the coated samples were washed with deionized water, air-dried, and further crystallized by annealing at 500°C for 20 min to form ZnO-NRs film.

2.2. Synthesis of SnO_2/ZnO-NRs films

A SnO_2 film was prepared using the spinning coating method. In a typical process, $SnCl_4 \cdot 5H_2O$ was dissolved in isopropyl alcohol (IPA) to create precursor solutions with concentrations of 0.01 M, 0.05 M. The precursor solution was then spin-coated onto the ZnO-NRs film, spun at 3000 rpm for 30 s, placed on a hot plate at 150°C for 20 min, and annealed at 500 °C in a tube furnace for 2h to produce a SnO_2-x/ZnO-NRs film, where x represents the SnO_2 precursor concentration. The term SnO_2/ZnO-NRs subsequently refers to SnO_2-0.01/ZnO-NRs, unless specified otherwise.

2.3. Fabrication of CABB/SnO_2/ZnO-NRs films

A CABB layer was deposited on ZnO-NRs or SnO_2-x/ZnO-NRs films using a vacuum evaporation system within a glovebox under a pressure below 10^{-4} Pa. CABB crystals were ground into powder as the source for evaporation, with the rate set at a constant 0.4 nm/s. The optimized final thickness was 50 nm. The samples were then heated on a hot plate in the glove box at 285°C for 10 min to create the CABB/ZnO-NRs or

CABB/SnO$_2$-x/ZnO-NRs film as the sensing layer. The term CABB/SnO$_2$/ZnO-NRs is used interchangeably with CABB/SnO$_2$-0.01/ZnO-NRs, unless specifically stated otherwise.

2.4. Fabrication and measurement of sensor device

The sensor was created by depositing platinum interdigital electrodes onto the sensing layer through DC magnetron sputtering, using a contact mask [29]. Gas sensing measurement were carried out in air at room temperature of 25°C and environmental humidity of 60%, if not particularly indicated. In this work, the NO$_2$ sample gas was purchased as premixed gas of 0.75% NO$_2$ with 99.25% Ar. The test chamber filled with ambient air is sealed, and the NO$_2$ sample gas is injected into the chamber via a syringe for the sensing test. Once the resistance is stabilized, the lid of the test chamber was opened to release the testing NO$_2$ gas. This is a traditional way for static gas sensing test. The sample gases CH$_4$, H$_2$, CO (5% CH$_4$, H$_2$, CO mixed with 95% Ar), NO, NO$_2$, SO$_2$ (0.75% NO, NO$_2$, SO$_2$ mixed with 99.25% Ar), H$_2$S (0.05% H$_2$S mixed with 99.95% SF$_6$), and NH$_3$, Ethanol, Acetone (bottled solution with saturated vapor pressure) are used for selectivity test. An external Keithly 2400 source meter connected to a computer was used to measure the sensor's resistance change, and the data were automatically recorded by the test system software. The test process is schematic shown in Fig. S1. The gas sensing response (Res) of the sensors is calculated by Eq. (1) below:

$$Res = \frac{R_{gas}}{R_{air}} - 1 \qquad (Eq.\,1)$$

where R_{gas} and R_{air} are the resistances of the sensors in NO$_2$ and in air respectively.

The response (τ_{res}) and recovery (τ_{recov}) times are defined as the time for the resistance change to reach up 90% of the final ΔR ($\Delta R = R_{air} - R_{gas}$). The selectivity factor (SF) is defined as the response ratio of the main gas (gas 1) to the comparison gas (gas 2):

$$SF = \frac{Res_{gas1}}{Res_{gas2}} \qquad (Eq.\,2)$$

Fig. 1 schematically illustrates the fabrication procedures and the test process of the CABB/SnO$_2$/ZnO-NRs sensor.
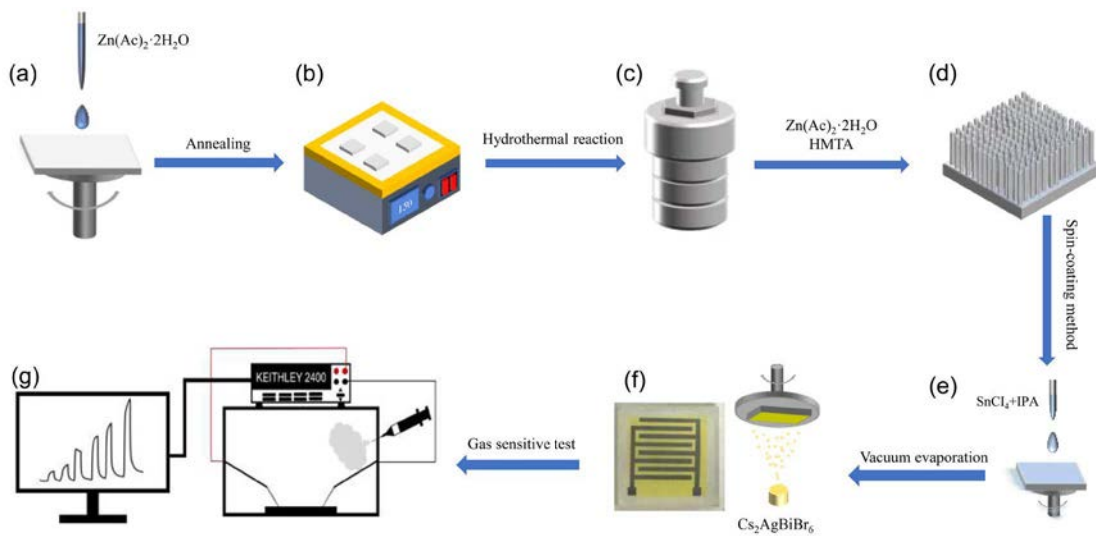

Fig. 1. Schematic showing the preparation and test procedures of the CABB/SnO$_2$/ZnO-NRs sensor.

(a) spin-coated ZnO seed layer; (b) hot table drying seed crystals; (c) hydrothermal reaction; (d) ZnO-NRs film; (e) spin-coated SnO$_2$ layer; (f) vacuum evaporation; and (g) gas test system.

2.5. Materials Characterization

The crystal structures of the samples were analyzed using x-ray diffractometry (XRD) with Cu-Kα radiation ($\lambda = 0.15418$ nm) on a Bruker D8 instrument. The morphology of the films was examined by field emission scanning electron microscopy (FESEM) using a Zeiss Sigma500 microscope. Ultraviolet-visible (UV–vis) diffuse reflectance

spectra were obtained using a Shimadzu UV-33600 spectrophotometer from Japan. Photoluminescence (PL) spectra were measured at room temperature with an excitation wavelength of 320 nm, employing a CLY18 Fluo Time 300 instrument from German PicoQuant. The element binding energy was determined by X–ray photoelectron spectroscopy obtained using the XPS Escalab 250Xi instrument from Thermo Fisher, USA with monochromatized Al Kα at the energy of 1486.6 eV as the X–ray source. The instrument was calibrated to the carbon C 1s peak at 248.8 eV present on the surface. The piezoelectric property of the films was measured by piezoelectric forces microscopy (PFM, SPA 400, Seiko Inc.).

3. Results and Discussions

3.1. Microstructure characterization

XRD analysis was employed to characterize the impact of interface engineering on the crystallinity of individual layers of the sensor. In the case of ZnO NRs, a distinct peak at approximately $2\theta = 34.46°$ signifies a well orientated alignment along the [0 0 2] direction (Fig. 2(a)). Noticeably, no discernible SnO_2-related peak appeared in the XRD spectra of SnO_2/ZnO-NRs, probably attributed to the even distribution and insufficient thickness of the SnO_2 film, falling beyond the detection limit. The minor peaks associated with (1 0 0), (1 0 1), and (1 0 2) ZnO plane in ZnO-NRs vanished when SnO_2 coating was applied on the surface. Furthermore, the (0 0 2) ZnO peak was found to shift to a higher diffraction angle with increasing SnO_2 precursor concentration, as evidenced in the magnified XRD patterns (Fig. 2(a)). This shift indicated the presence

of compressive stress along the [0 0 2] direction of ZnO-NRs, leading to alterations in the polarization electric field within the ZnO nanorods. Fig. 2(b) shows the XRD patterns of CABB/SnO$_2$/ZnO-NRs, where the additional diffraction peaks correspond well with the standard Cs$_2$AgBiBr$_6$, confirming the successful synthesis of CABB on the SnO$_2$/ZnO-NRs.
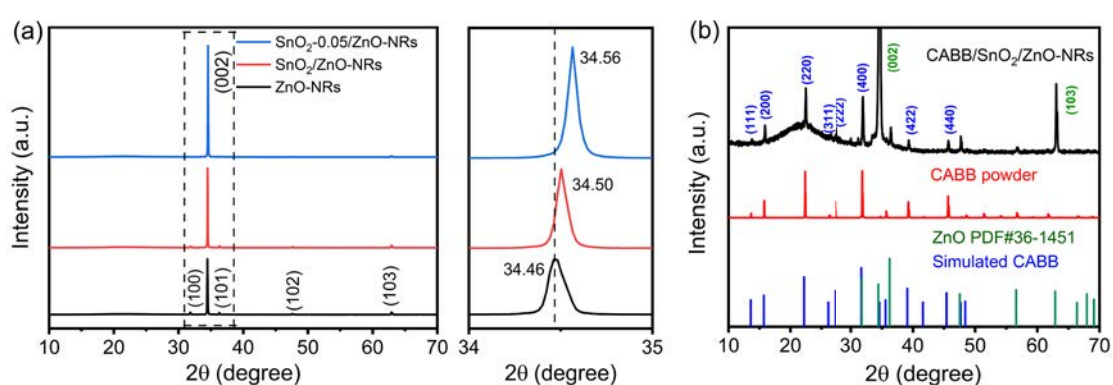

Fig. 2. (a) XRD patterns (left) and amplified local region of the XRD patterns (right) of the ZnO-NRs and SnO$_2$-x/ZnO-NRs; (b) XRD patterns of CABB/SnO$_2$/ZnO-NRs.

The SEM images in Fig. 3 show the morphologies of the ZnO-NRs, SnO$_2$/ZnO-NRs, and CABB/SnO$_2$/ZnO-NRs films. In Fig. 3(a), the hexagonal ZnO nanorods, each with an average diameter of 260 nm, were closely arranged and grown along the C-axis orientation of ZnO, consistent with the XRD pattern in Fig. 2(a). The surface of ZnO-NRs coated with 0.01 M SnO$_2$ exhibits a rough structure in Fig. 3(b). As the SnO$_2$ precursor concentration increased to 0.05 M, the nanorods transform into a cylindrical shape, with SnO$_2$ nanocrystals covering the top and sides in Fig. 3(c). In addition, some SnO$_2$ forms a network of interconnected bridges among the ZnO nanorods. Figs. 3(d)

and 3(e) reveal that the average length of the nanorods is 2.9 μm, and that the SnO$_2$/ZnO-NRs are uniformly covered by CABB layer.
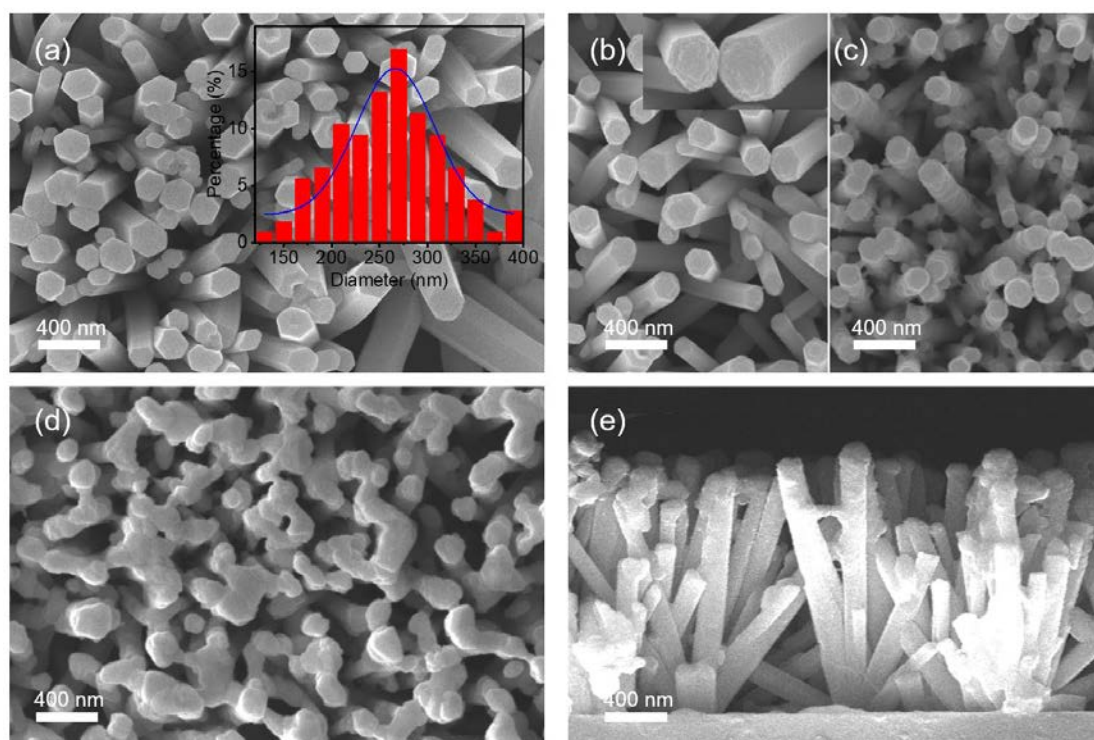

Fig. 3. SEM images showing the morphology of (a) ZnO-NRs; (b) SnO$_2$/ZnO-NRs; (c) SnO$_2$-0.05/ZnO-NRs; and (d, e) CABB/SnO$_2$/ZnO-NRs with (d) and (e) being the top and cross-sectional view, respectively.

Fig. 4(a) shows the optical absorption properties measured by UV–Vis spectroscopy. The absorption edge around 400 nm for ZnO-NRs corresponds to the optical band gap of ZnO, and the much increased absorption in the visible region is attributed to the light scattering of the nanorods. To elucidate the optical properties without interference from ZnO-NRs, the CABB is also evaporated onto quartz. The consistent absorption peak positions imply that the CABB layer on SnO$_2$/ZnO-NRs shares the same optical band gap as on quartz. CABB is classified as an indirect-gap semiconductor, and its optical bandgap E$_g$ can be obtained from the optical absorption spectrum (the inserted plots in

Fig. 4(a)) by the following equation:

$$\alpha = \frac{c(hv - E_g \pm E_p)^2}{exp(\pm E_p / kT - 1)}, \, hv > E_g \mp E_p \qquad (Eq. \ 3)$$

$$= 0, \, hv \leq E_g \mp E_p$$

The estimated E_g of the CABB layer is 2.44 eV, and the phonon energy (E_p) is 0.05 eV. The band gap value is aligned with the previously reported value of 2.39 eV for the CABB film [30].

The photoluminescence (PL) spectrum of ZnO-NRs in Fig. 4(b) displays three emission peaks at 390 nm, 470 nm, and 610 nm, corresponding to the near-band edge emission (NBE), emission from the donor level of Zn interstitial to acceptor energy level of Zn vacancy, and the ionized oxygen vacancies, respectively. The intensity of the Zn and oxygen vacancies-related peak was found to decrease when SnO_2 coating is on ZnO-NRs and CABB coating is on SnO_2/ZnO-NRs, indicating the formation of heterojunction among ZnO-NRs, SnO_2, and CABB. The build-in electric field at the heterojunction interface enhances the separation of photon-generated carriers and diminishes the radiative recombination.
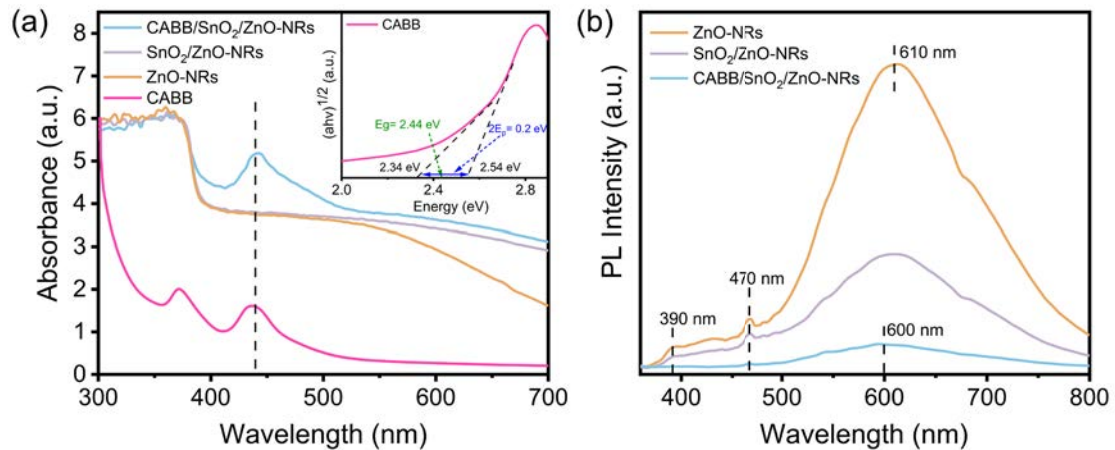

Fig. 4. (a) UV–vis absorption spectra; and (b) PL spectra of ZnO-NRs, SnO_2/ZnO-NRs, and

CABB/SnO$_2$/ZnO-NRs.

The XPS survey scan of CABB/SnO$_2$/ZnO-NRs is shown in Fig. 5(a), and high-resolution XPS spectra of the elements are conducted to determine their chemical states (Figs. 5(b)-5(d)). The O 1s spectrum of ZnO-NRs in Fig. 5(b) can be deconstructed into three peaks, positioned at 530.27, 531.54, and 532.57 eV, corresponding to lattice oxygen (O$_L$), oxygen vacancies (O$_V$), and adsorbed water molecules (H–O–H), respectively [31]. The O$_V$ content is 38.74%, 42.82%, 34.47%, and 34.81% for ZnO-NRs, SnO$_2$/ZnO-NRs, SnO$_2$-0.05/ZnO-NRs, and CABB/SnO$_2$/ZnO-NRs, respectively. This indicates that a low concentration (0.01 M) of SnO$_2$ primarily induces surface defects (the roughness on the surface observed in Fig. 3(b)) and increases the oxygen vacancy density. Conversely, a high concentration of SnO$_2$ (0.05 M) produces thicker SnO$_2$ layer covering the surface area of ZnO-NRs, thereby decreasing the oxygen vacancy density. The CABB coating on the SnO$_2$/ZnO-NRs surface also diminishes the oxygen vacancy density.

The Zn 2p XPS spectrum of ZnO-NRs (Fig. 5(c)) shows two peaks, Zn 2p$_{1/2}$ and 2p$_{3/2}$, at 1044.62 eV and 1021.52 eV, respectively. The Zn 2p$_{3/2}$ peak experiences a blue shifts of about 0.22 eV in SnO$_2$/ZnO-NRs and 0.55 eV in CABB/SnO$_2$/ZnO-NRs, suggesting charges transfer away from Zn sites. The Sn 3d XPS spectra in Fig. 5(d) display a similar blue shift of the Sn 3d peaks. The peaks at 486.71 and 495.21 eV in SnO$_2$/ZnO-NRs can be attributed to Sn 3d$_{5/2}$ and Sn 3d$_{3/2}$, respectively, corresponding to Sn^{4+} cations. The core level of Sn 3d$_{5/2}$ experiences a blue shift by 0.26 eV in

CABB/SnO$_2$/ZnO-NRs, indicating a movement of charges away from Sn sites. The comparable blue shift of Zn 2p and Sn 3d peaks suggests a strong interaction between ZnO-NR$_S$, SnO$_2$ and the CABB species.
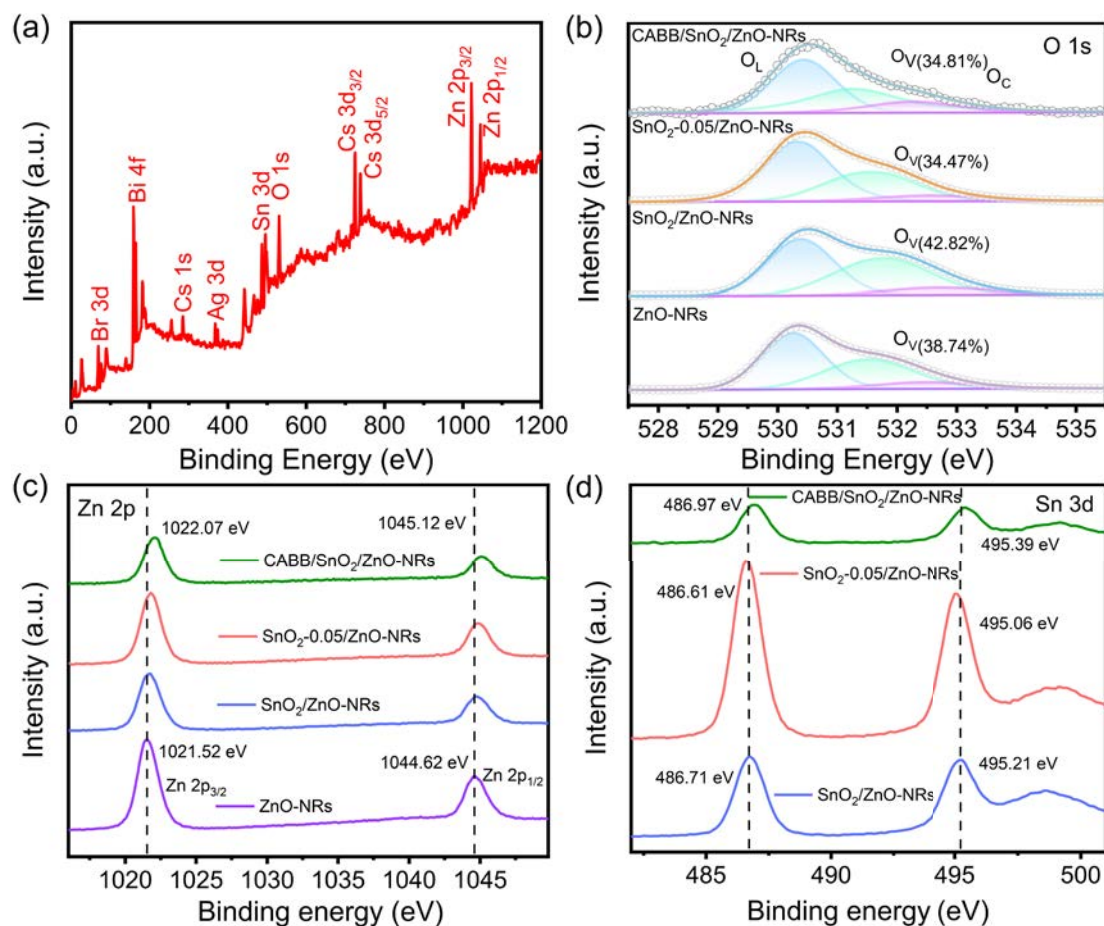

Fig. 5. XPS spectra: (a) survey scan of CABB/SnO$_2$/ZnO-NRs; (b) O 1s; (c) Zn 2p; (d) Sn 3d.

4.2. NO$_2$ gas sensing properties

The performance of NO$_2$ sensing was assessed at room temperature of 25°C with a relative humidity of 60%. Both ZnO-NRs and SnO$_2$/ZnO-NRs show noticeable response to NO$_2$ (Fig. 6(a)). The initial resistance is about 24 MΩ for ZnO-NRs, and such a high resistance is unfavorable for the real application of gas sensor. The initial resistance decreases about 10 times in SnO$_2$/ZnO-NRs, and further decreases around 100 times to 300 kΩ in CABB/SnO$_2$/ZnO-NRs. The dynamic resistance changes of

CABB/SnO$_2$/ZnO-NRs (CABB/SnO$_2$-0.05/ZnO-NRs) under various NO$_2$ concentrations in Fig. 6(b) (Fig. S2) indicate a significant improvement in sensing performance after CABB deposition. CABB/SnO$_2$/ZnO-NRs demonstrated the best response and the shortest response/recovery time compared to ZnO-NRs, SnO$_2$/ZnO-NRs, and CABB/SnO$_2$-0.05/ZnO-NRs (Figs. 6(c) - 6(e)). The response at 100 ppm was 9.66, about 5.5 times higher than that of SnO$_2$/ZnO-NRs, with a response/recovery time of 8s/9s, demonstrating rapid response and recovery characteristics. Fig. 6(f) shows the response curves under 1 ppm NO$_2$ condition for 6 cycles, showcasing the excellent baseline stability and response repeatability. The baseline goes up under high concentration conditions. Fig. 6(g) displays the changes in resistance and response under various humidity conditions at 25°C. The resistance slightly increase as increasing the humidity, and the response is 2.07 ± 0.11 with 5% deviation under various relative humidity, indicating good humidity resistance. The selectivity for reference gases is measured and shown in Fig. 6(h). The sample exhibited no response to CH$_4$, CO, and H$_2$, even at concentrations as high as 400 ppm, while it had a weak response to H$_2$S, SO$_2$ and NO. The sensor responds more strongly to NH$_3$ than to other interfering gases, and the selectivity factor (SF) for NO$_2$ to NH$_3$ is 11, showing a great selectivity to NO$_2$. Traditional perovskite-based gas sensors have poor stability and are easily decomposed in an air environment, so most perovskite-based gas sensors are tested under the protection of a specific gas environment, such as N$_2$ or Ar [25, 27, 32]. In this work, the response of CABB/SnO$_2$/ZnO-NRs sensors was still about 70% of that of the newly prepared ones after storing in the air for 20 days without any preservation

(Fig. 6(i)), showing a significant improvement in stability compared with CABB/ZnO-NRs sensors which are stable only in less than a day (Fig. S3). It is believed that the stability could be further improved if the SnO_2 layer is optimized in terms of microstructure and a suitable package is added to protect the device from light illumination.
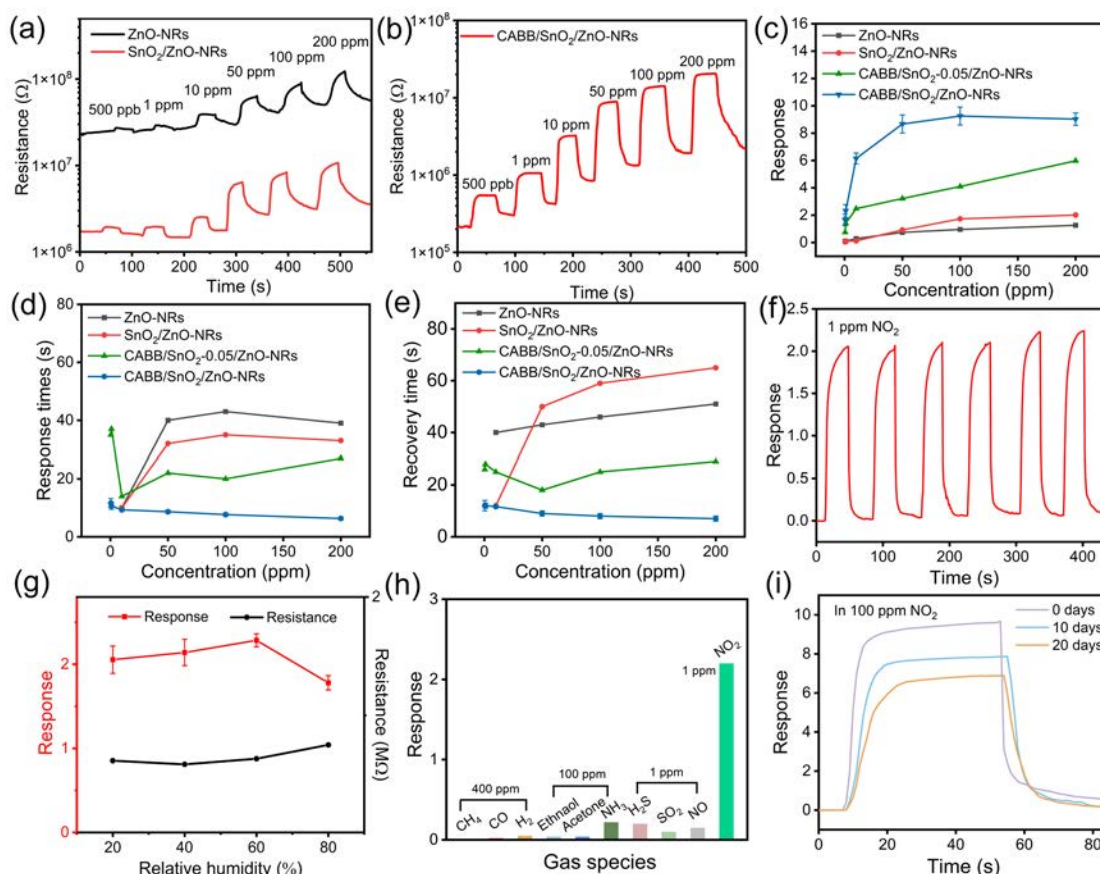

Fig. 6. The dynamic resistance of (a) ZnO-NRs and SnO_2/ZnO-NRs; (b) CABB/SnO_2/ZnO-NRs; (c) the response, (d) response time and (e) recovery time of the device as a function of gas concentration; (f) repeatability at 1 ppm NO_2. (g) humidity test at 25°C; (h) the selectivity to various gases; (i) long-term stability test.

The NO_2 sensing performance of CABB/SnO_2/ZnO-NRs was compared with other metal halide perovskite materials reported in previous studies as shown in Table. 1. The

sensor developed in this work can operate in air under various humidity without the need for additional light assistance, demonstrating excellent response and fast response speed. This makes it a most promising candidate for industry application.

Table. 1. Comparison of NO$_2$ gas sensing properties with other metal halide perovskite materials in previous reports at different operating conditions.

Materials	Environment	T (℃)	C (ppm)	Response (R_{gas}/R_{air}-1)	Response/ Recovery time (s)	Ref.
CH$_3$NH$_3$PbI$_3$ film	In Ar	R.T	1	2.3	22/13 s	[25]
CsCuI$_3$ film	In N$_2$	R.T	0.1	2.2	146/413 s	[32]
Cs$_2$SnI$_6$ film	In dry air	R.T	20	34	247/818 s	[33]
CsPbBr$_3$ film	In air	R.T.	8	0.26	58/77 s	[26]
MASnI$_3$ film	405nm LED In N$_2$	R.T	1	40	200/600 s	[34]
CsPbBr$_3$/ZnO powder	520nm LED In air	R.T.	5	52	63/40 s	[27]
Cs$_2$AgBiBr$_6$/SnO$_2$/ ZnO film	In air	R.T.	1	2.3	12/9 s	This work

*All the response values are from the reference and recalculated based on the same definition (R_{gas}/R_{air}-1), and all the response/recovery time is defined as the time for the resistance to reach up to 90% of the final ΔR ($\Delta R = R_{air} - R_{gas}$).

4.3. Gas sensing mechanism

Fig. 7(a) shows the evolution of color in CABB/ZnO-NRs over time under argon within the glove box. The yellow hue exhibits no discernable alteration in the argon atmosphere stored for 180 days, indicating stability of the CABB layer. Conversely, in ambient air, the color of the composite film gradually diminished within a short duration (several hours) (Fig. 7(b)). The CABB layer, deposited on the ZnO seed layer comprised of disordered small nanocrystals, maintains its color stability even when

exposed to air for 40 days (Fig. 7(b)). Furthermore, when CABB is coated on SnO$_2$/ZnO-NRs, the color remains unchanged after being stored in air for 180 days (Fig. 7(c)). CABB/SnO$_2$/ZnO-NRs with electrodes in ambient air for 40 days also show no color change. This suggests that the introduction of SnO$_2$ layer significantly enhances the stability of CABB on ZnO-NRs.
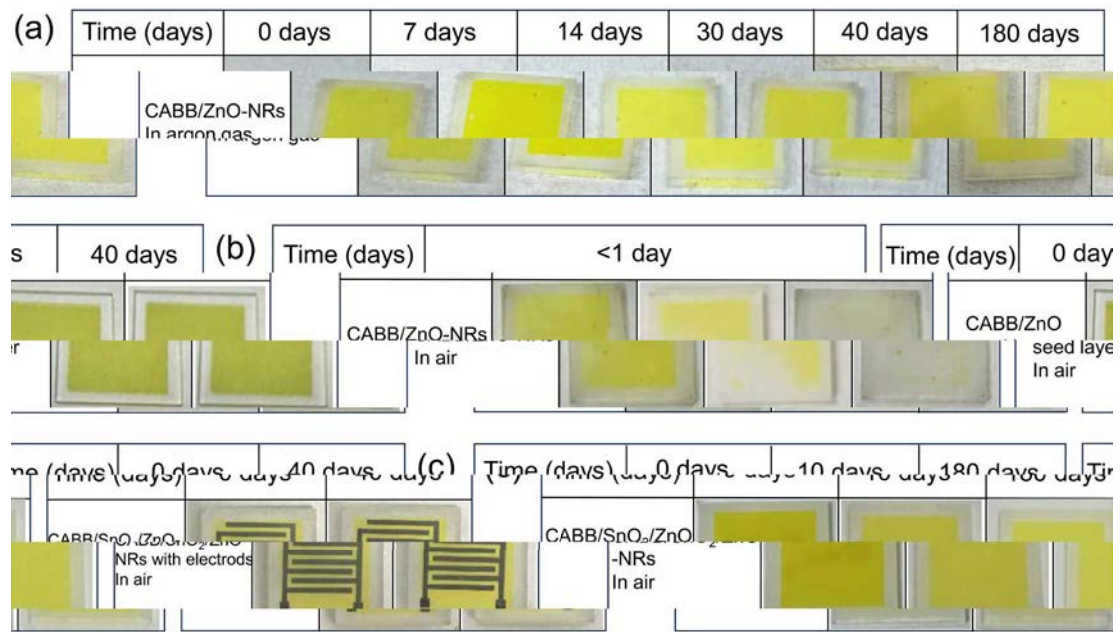

Fig. 7. Evolution of the color with time of (a) CABB/ZnO-NRs in argon gas within a glove box, (b) CABB/ZnO-NRs and CABB/ZnO seed layer in ambient air, and (c) CABB/SnO$_2$/ZnO-NRs and CABB/SnO$_2$/ZnO-NRs with electrods in ambient air.

To elucidate these phenomena, the piezoelectric property of the samples was characterized using piezoelectric forces microscopy (PFM) as depicted in Fig. 8. In PFM measurements, an AC voltage (V) was applied to the thin film surface and the electrode at the bottom through the conductive tip, deforming the surface underneath the tip. The distinctive butterfly-shaped loops (Fig. 8(a)) and the average phase angle close to 180° (Fig. 8(b)), specifically measuring 174°, 175°and 179°, for ZnO-NRs,

SnO$_2$/ZnO-NRs and SnO$_2$-0.05/ZnO-NRs, respectively, signify the presence of the piezoelectric effect rather than electrostatic forces. The corresponding PFM images are shown in Fig. 8(c-e). The piezoelectric coefficient d$_{33}$ is the conversion coefficient for converting the deformation energy into electric energy, reflecting the coupling relationship between piezoelectric materials' elastic and dielectric properties. The average d$_{33}$ value is 2.27 pm V^{-1}, and this value increases to 3.65 pm V^{-1} and 4.84 pm V^{-1} for SnO$_2$/ZnO-NRs and SnO$_2$-0.05/ZnO-NRs, respectively. This trend aligns with the observed compressive stress along the c-axis in ZnO-NRs, which intensifies with an increase in the SnO$_2$ precursor concentration (Fig. 2(a)). The lattice strain induces permanent local electric dipoles, resulting in the enhancement of the piezoelectric polarization (d$_{33}$) in SnO$_2$/ZnO-NRs. Our previous publication [35] have shown a piezoelectric polarization-enhanced gas sensing. It was demonstrated that the enhanced polarization electric field provides additional energy to the electrons, just like additional heating or illumination, to overcome the reaction energy barriers, thus enhancing the gas sensing performance. However, the CABB degradation rate is reduced after the insert of the SnO$_2$ layer, indicating that the polarization field is the reason for the enhancement of response but not the reason for the CABB degradation. In addition, despite the larger polarization field, SnO$_2$-0.05/ZnO-NRs exhibit a poorer NO$_2$ gas response than SnO$_2$/ZnO-NRs after the CABB coating. It is possible that the SnO$_2$ interconnected bridges among the ZnO nanorods in the SnO$_2$-0.05/ZnO-NRs make the current not only along the ZnO-NRs, but also between the NRs, which reduces the gas response.
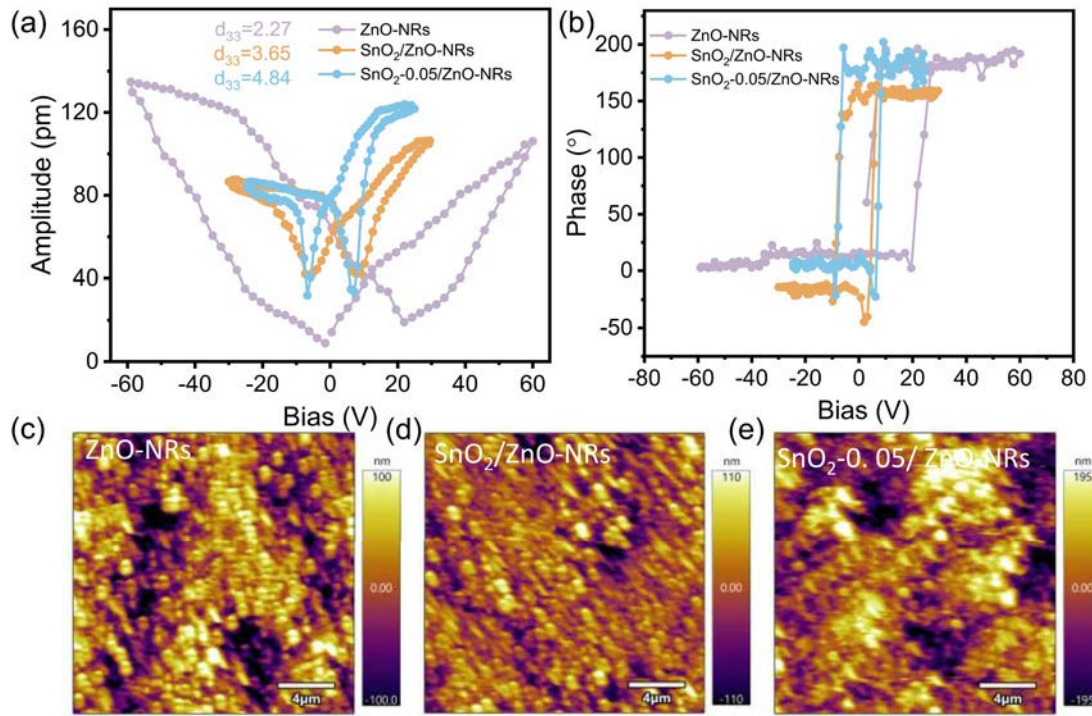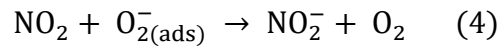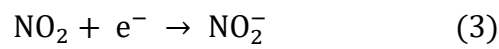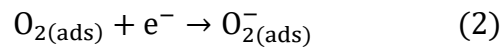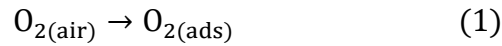
Fig. 8. (a) A representative amplitude by PFM versus applied bias voltage curve; (b) phase-voltage hysteresis loop versus applied bias voltage curve; (c-e) PFM images of domain structures ZnO-NRs, SnO_2/ZnO-NRs and SnO_2-0.05/ZnO-NRs films.

In order to understand the impact of the incorporated SnO_2 layer on the stability of CABB and its improved gas sensing performance, the energy band structures of ZnO-NRs, SnO_2 and CABB are established by considering the optical band gap (Fig. 4), the valence band edge (Fig. S5) and the work functions [29, 36, 37] of distinct layers presented in Fig. S6. The band structures for the CABB/ZnO-NRs and the CABB/SnO_2/ZnO-NRs hetrojunction are established by aligning individual ones with the Fermi level, as shown in Fig. 9(a) and Fig. 9(b). At the interface between CABB and ZnO-NRs, a straddling gap (type I) structure is evident, indicating the migration of

both electron and holes from ZnO to CABB. This leads to a strong redox reaction on the CABB surface, rendering it prone to decomposition, akin to the photo-corrosion of CdS [38, 39]. Inserting a layer of SnO_2 between ZnO-NRs and CABB introduces a step in the conduction band (CB) of SnO_2, facilitating the smooth electron transfer from ZnO to CABB and the accumulation of charges at the CABB. In contrast, the valence band (VB) of SnO_2 effectively hinders the migration of holes from ZnO-NRs to CABB, preventing the redox reaction and notably enhancing the stability of the CABB layer. The mechanism of the gas sensing can be understood based on the aforementioned analysis, attributed to the enhancement of the polarization electric field on the CABB surface promoting gas absorption. All the three layers, ZnO, SnO_2 and CABB, exhibit N-type semiconductor properties. Upon exposure to the ambient air, oxygen molecules seize electrons in the semiconductor's conduction band, forming adsorbed oxygen negative ions (O_2^-), and consequently creating a depletion layer on the semiconductor surface. According to the energy band structure (Fig. 9(b)), the depleting layer exists not only at the surface but also at the interface between different layers. In the $CABB/SnO_2/ZnO$-NRs structure, a higher density of O_2^- is formed on the CABB compared to SnO_2/ZnO-NRs, as more electrons accumulate on the former. NO_2, with a higher oxidization ability, is easily to replace the chemically adsorbed O_2^- on the surface, resulting in more electrons transferring toward NO_2 molecules and the formation of chemically adsorbed NO_2^-. This increases the width of the depletion layers at the $CABB/air$, $CABB/SnO_2$ and SnO_2/ZnO interfaces, thus significantly enhancing the sensor resistance (Fig. 9(c)). Upon removal from the NO_2 environment, NO_2^-

dissociates from the surface by the driving of concentration gradient, releasing electrons back into the conduction band. Oxygen around occupies the NO_2^- sites again, resulting in a decrease in the resistance of the composite film. The corresponding reaction equations are present below [27]:

$$O_{2(air)} \rightarrow O_{2(ads)} \qquad (1)$$

$$O_{2(ads)} + e^- \rightarrow O_{2(ads)}^- \qquad (2)$$

$$NO_2 + e^- \rightarrow NO_2^- \qquad (3)$$

$$NO_2 + O_{2(ads)}^- \rightarrow NO_2^- + O_2 \qquad (4)$$

The polarization electric field provides the required energy for the O_2 and NO_2 to extract electrons from the CABB and enhances the chemically adsorption on the surface. The inserted SnO_2 layer allows only electrons to transfer to the CABB, increasing the carrier concentration, and promoting the migration speed, thus improving gas adsorption and desorption rates and enhancing the sensing response and speed.

In addition, it has been reported that Ag and Br ions are prone to migrate vacancy-mediated in the CABB, leaving more defects on the surface [30]. The state of surface defects may change or redistribute when a high concentration of NO_2 is adsorbed on the surface. This requires higher activation energy for NO_2 dissociation from the surface, reducing the rate of NO_2 dissociation. The residue amount of NO_2^- on the surface increases as the concentration increases, boosting the recovered resistance to a level higher than the initial value and resulting in the baseline fluctuation at high concentration. It is possible to passive the CABB surface by N-heterocyclic amines [40], reducing the formation of vacancies and thus suppressing the baseline fluctuation.
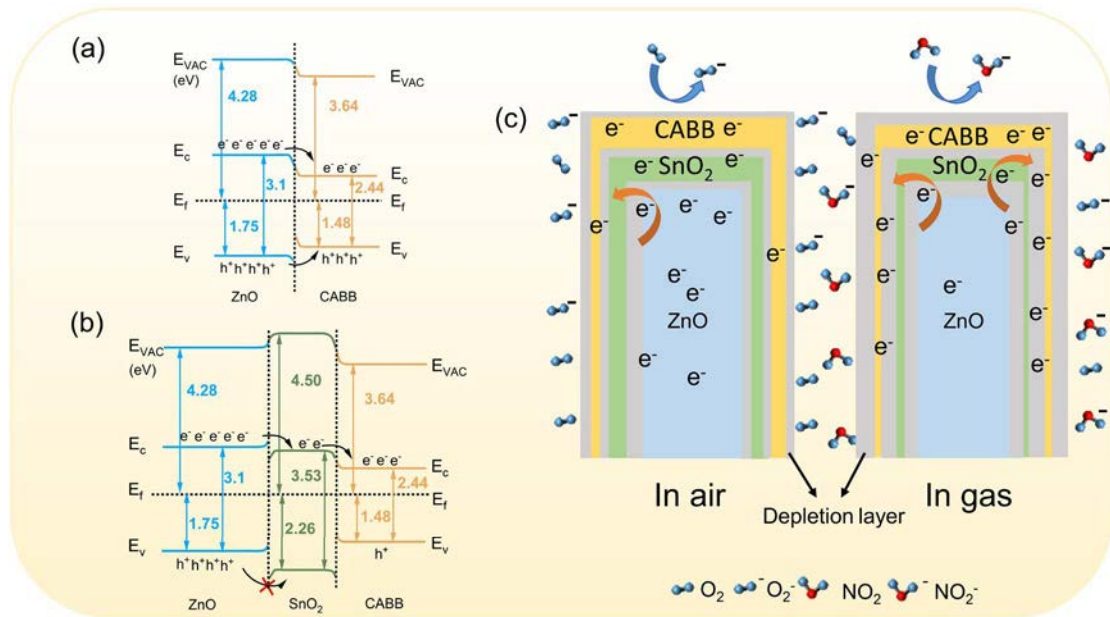
Fig. 9. (a) Schematic of energy alignment diagram of (a) CABB/ZnO-NRs and (b) CABB/SnO$_2$/ZnO-NRs; (c) The schematic illustration showing the mechanism of gas sensing.

5. Conclusions

We developed a sensor to detect NO$_2$ using a lead-free perovskite-based CABB/SnO$_2$/ZnO-NRs system. It was found that CABB is unstable and prone to decomposition on the ZnO-NRs due to the migration of both electrons and holes to CABB, resulting in a robust redox reaction. To address this issue, a SnO$_2$ layer was spin-coated at the interfaces of ZnO-NRs and CABB perovskite layer, serving as an effective hole-blocking layer that significantly improved the stability of the CABB and, consequently, the performance of the sensor device. Furthermore, the SnO$_2$ coating on

ZnO-NRs enhances the polarization effect, effectively promoting the chemical adsorption rate and significantly improving the sensing performance. The optimized CABB/SnO$_2$/ZnO-NRs sensor demonstrates superior gas-sensing capabilities with high response and rapid response/recovery speed across the entire concentration range. Remarkably, it can work at room temperature without additional heat or light assistance. This innovative approach can pave the way for the development of lead-free perovskite-based devices for various sensing applications, contributing to environmental monitoring.

Declaration of Competing Interest

The authors declare no conflict of interest.

Acknowledgement

References

[1] L. Ma, S. Chen, W. Yan, G. Zhang, Y. Ying, H. Huang, D. Ho, W. Huang, C. Zhi, A high-energy aqueous Zn‖NO$_2$ electrochemical cell: a new strategy for NO$_2$ fixation and electric power generation, Energy Environ. Sci. 16 (2023) 1125-1134. http://doi.org/10.1039/d2ee03749a.

[2] S. Kumar, V. Pavelyev, P. Mishra, N. Tripathi, P. Sharma, F. Calle, A review on 2D transition metal di-chalcogenides and metal oxide nanostructures based NO$_2$ gas sensors, Mater. Sci. Semicond. Process. 107 (2020) 104865. http://doi.org/10.1016/j.mssp.2019.104865.

[3] S. S. Shendage, V.L. Patil, S. A. Vanalakar, S. P. Patil, N. S. Harale, J. L. Bhosale, J. H. Kim, P. S. Patil, Sensitive and selective NO_2 gas sensor based on WO_3 nanoplates, Sens. Actuators B Chem. 240 (2017) 426-433. http://doi.org/10.1016/j.snb.2016.08.177.

[4] D. Li, D. Han, Y. Chen, Z. Liu, X. Liu, L. Liu, X. Han, X. He, S. Sang, Hollow porous GaN nanofibers gas sensor for superior stability and sub-ppb-level NO_2 gas detection, Sens. Actuators B Chem. 371 (2022) 132583. http://doi.org/10.1016/j.snb.2022.132583.

[5] S. C. Anenberg, A. Mohegh, D. L. Goldberg, G. H. Kerr, M. Brauer, K. Burkart, P. Hystad, A. Larkin, S. Wozniak, L. Lamsal, Long-term trends in urban NO(2) concentrations and associated paediatric asthma incidence: estimates from global datasets, Lancet Planet Health. 6 (2022) e49-e58. http://doi.org/10.1016/S2542-5196(21)00255-2.

[6] H. Li, L. Chen, Z. Guo, N. Sang, G. Li, In vivo screening to determine neurological hazards of nitrogen dioxide (NO_2) using Wistar rats, J. Hazard. Mater. 225-226 (2012) 46-53. http://doi.org/10.1016/j.jhazmat.2012.04.063.

[7] Y. Tang, Y. Zhao, H. Liu, Room-Temperature Semiconductor Gas Sensors: Challenges and Opportunities, ACS Sens. 7 (2022) 3582-3597. http://doi.org/10.1021/acssensors.2c01142.

[8] L. Liu, C. Mao, H. Fu, X. Qu, S. Zheng, ZnO Nanorod-Immobilized Pt Single-Atoms as an Ultrasensitive Sensor for Triethylamine Detection, ACS Appl. Mater. Interfaces. 15 (2023) 16654-16663. http://doi.org/10.1021/acsami.2c21410.

[9] H. Cao, Z. Hu, X. Wei, H. Wang, X. Tian, S. Ding, Conductometric ethanol gas sensor based on a bilayer film consisting of SnO_2 film and $SnO_2/ZnSnO_3$ porous film prepared by magnetron sputtering, Sens. Actuators B Chem. 382 (2023) 133562. http://doi.org/10.1016/j.snb.2023.133562.

[10] V. Navakoteswara Rao, P. Kedhareswara Sairam, M. D. Kim, M. Rezakazemi, T. M. Aminabhavi, C. W. Ahn, J. M. Yang, CdS/TiO_2 nano hybrid heterostructured materials for superior hydrogen production and gas sensor applications, J. Environ. Manage. 340 (2023) 117895. http://doi.org/10.1016/j.jenvman.2023.117895.

[11] S. Ananthi, M. Kavitha, A. Balamurugan, E. Ranjith Kumar, G. Magesh, A. F. Abd El-Rehim, C. Srinivas, P. Anilkumar, J. Suryakanth, C. Sharmila Rahale, Synthesis, analysis and characterization of camellia sinensis mediated synthesis of NiO nanoparticles for ethanol gas sensor applications, Sens. Actuators B Chem. 387 (2023) 133742. http://doi.org/10.1016/j.snb.2023.133742.

[12] K. Sun, G. Zhan, L. Zhang, Z. Wang, S. Lin, Highly sensitive NO_2 gas sensor based on ZnO nanoarray modulated by oxygen vacancy with Ce doping, Sens. Actuators B Chem. 379 (2023) 133294. http://doi.org/10.1016/j.snb.2023.133294.

[13] L. Zhao, R. Jin, C. Wang, T. Wang, Y. Sun, P. Sun, G. Lu, Flower-like $ZnO-Co_3O_4$ heterojunction composites for enhanced acetone sensing, Sens. Actuators B Chem. 390 (2023) 133964. http://doi.org/10.1016/j.snb.2023.133964.

[14] X. Liu, T. Ma, N. Pinna, J. Zhang, Two-Dimensional Nanostructured Materials for Gas Sensing, Adv. Funct. Mater. 27 (2017) 1702168. http://doi.org/10.1002/adfm.201702168.

[15] B. Maji, B. Barik, S.J. Sahoo, L.S.K. Achary, K. Kumar Sahoo, J.P. Kar, P. Dash, Shape selective comprehensive gas sensing study of different morphological manganese-cobalt oxide based nanocomposite as potential room temperature hydrogen gas sensor, Sens. Actuators B Chem. 380 (2023) 133348. http://doi.org/10.1016/j.snb.2023.133348.

[16] H. Li, C. Chen, H. Hu, Y. Li, Z. Shen, F. Li, Y. Liu, R. Liu, J. Chen, C. Dong, S. Mabrouk, R.S. Bobba, A. Baniya, M. Wang, Q. Qiao, Strategies for high-performance perovskite solar cells from materials, film engineering to carrier dynamics and photon management, InfoMat. 4 (2022) 12322. http://doi.org/10.1002/inf2.12322.

[17] T. Luo, G. Ye, X. Chen, H. Wu, W. Zhang, H. Chang, F-doping-Enhanced Carrier Transport in the SnO_2/Perovskite Interface for High-Performance Perovskite Solar Cells, ACS Appl. Mater. Interfaces. 14 (2022) 42093-42101. http://doi.org/10.1021/acsami.2c11390.

[18] C. Xie, C.K. Liu, H.L. Loi, F. Yan, Perovskite-Based Phototransistors and Hybrid Photodetectors, Adv. Funct. Mater. 30 (2020) 1903907. http://doi.org/10.1002/adfm.201903907.

[19] E. A. R. Assirey, Perovskite synthesis, properties and their related biochemical and industrial application, Saudi Pharm J. 27 (2019) 817-829. http://doi.org/10.1016/j.jsps.2019.05.003.

[20] X. L. Xu, X. P. Wang, W. W. Liu, S. Y. Wang, H. T. Jiang, S. Y. Ma, U. F. Yuan, N. A. Ma, Ambient Stable $CsPbBr_3$/ZnO Nanostructures for Ethanolamine Sensing, Acs Appl. Nano Mater. 5 (2022) 15030-15041. http://doi.org/10.1021/acsanm.2c03227.

[21] W. Xuan, H. Shan, D. Hu, L. Zhu, T. Guan, Y. Zhao, Y. Qiang, J. Song, J. Zhang, M. Sui, X. Gu, S. Huang, In-situ synthesis of stable ZnO-coated $CsPbBr_3$ nanocrystals for room- temperature heptanal sensors, Mate. Today Chem. 26 (2022) 101155. http://doi.org/10.1016/j.mtchem.2022.101155.

[22] D. I. Markina, S. S. Anoshkin, M. A. Masharin, S. A. Khubezhov, I. Tzibizov, D. Dolgintsev, I. N. Terterov, S. V. Makarov, A. P. Pushkarev, Perovskite Nanowire Laser for Hydrogen Chloride Gas Sensing, ACS Nano. 17 (2023) 1570-1582. http://doi.org/10.1021/acsnano.2c11013.

[23] M. Shellaiah, K. W. Sun, Review on Sensing Applications of Perovskite Nanomaterials, Chemosensors. 8 (2020) 55. http://doi.org/10.3390/chemosensors8030055.

[24] A. K. Singh, S. Singh, V. N. Singh, G. Gupta, B. K. Gupta, Probing reversible photoluminescence alteration in $CH_3NH_3PbBr_3$ colloidal quantum dots for luminescence-based gas sensing application, J. Colloid Interface Sci. 554 (2019) 668-673. http://doi.org/10.1016/j.jcis.2019.07.054.

[25] X. W. Fu, S. L. Jiao, N. Dong, G. Lian, T. Y. Zhao, S. Lv, Q. L. Wang, D. L. Cui, A $CH_3NH3PbI_3$ film for a room-temperature NO_2 gas sensor with quick response and high selectivity, Rsc Adv. 8 (2018) 390-395. http://doi.org/10.1039/c7ra11149e.

[26] J. Kim, L. Hu, H. Chen, X. Guan, P. R. Anandan, F. Li, J. Tang, C.-H. Lin, K. Kalantar-Zadeh, A. Tricoli, T. Wu, P-type Charge Transport and Selective Gas

Sensing of All-Inorganic Perovskite Nanocrystals, ACS Materials Lett. 2 (2020) 1368-1374. http://doi.org/10.1021/acsmaterialslett.0c00346.

[27] Y. Li, S. Sun, Y. Wang, F. Liu, H. Wang, J. Bai, M. Lu, G. Lu, $CsPbBr_3$ quantum dots enhanced ZnO sensing to NO_2 at room temperature, Sens. Actuators B Chem. 368 (2022) 132189. http://doi.org/10.1016/j.snb.2022.132189.

[28] W. Ye, L. Zhao, H. Z. Lin, L. Ding, Q. Cao, Z. K. Chen, J. Wang, Q. M. Sun, J. H. He, J. M. Lu, Halide Perovskite glues activate two-dimensional covalent organic framework crystallites for selective NO(2) sensing, Nat. Commun. 14 (2023) 2133. http://doi.org/10.1038/s41467-023-37296-0.

[29] T. Tan, Z. Hang, X. Li, S. Wang, K. Homewood, X. Xia, Y. Bao, Y. Gao, Ultra-high-response heat free H_2 sensor based on a WO_3/Pt-ZnO thin film, J. Alloy. Compd. 979 (2024) 173527. http://doi.org/10.1016/j.jallcom.2024.173527.

[30] M. Ghasemi, L. Zhang, J. H. Yun, M. Hao, D. He, P. Chen, Y. Bai, T. Lin, M. Xiao, A. Du, M. Lyu, L. Wang, Dual-Ion-Diffusion Induced Degradation in Lead-Free $Cs_2AgBiBr_6$ Double Perovskite Solar Cells, Adv. Funct. Mater. 30 (2020) 2002342. http://doi.org/10.1002/adfm.202002342.

[31] J. Li, M. Zheng, M. Yang, X. Zhang, X. Cheng, X. Zhou, S. Gao, Y. Xu, L. Huo, Three-in-one Ni doped porous SnO_2 nanorods sensor: Controllable oxygen vacancies content, surface site activation and low power consumption for highly selective NO_2 monitoring, Sens. Actuators B Chem. 382 (2023) 133550. http://doi.org/10.1016/j.snb.2023.133550.

[32] X. Sun, J. Yang, Z.L. Wu, G. Meng, X.Z. Guo, D.L. Kuang, L. Xiong, W.J. Qu, X.D. Fang, X. Yang, X.S. Tang, Y. He, Lead-Free $CsCu_2I_3$ Perovskite Nanostructured Networks Gas Sensor for Selective Detection of Trace Nitrogen Dioxide at Room Temperature, Ieee Sens J. 21 (2021) 14677-14684. http://doi.org/10.1109/jsen.2021.3071744.

[33] H. Pham Tien, H. Phung Dinh, N. Tien-Anh, T. Pham Van, H. Vu Xuan, L. Hyo-Jun, L. Sangwook, L. Joon-Hyung, H. Young-Woo, Growth and NO_2 sensing properties of Cs_2SnI_6 thin film, Mater. Res. Bull. 147 (2021) 111628. http://doi.org/10.1016/j.materresbull.2021.111628.

[34] V. X. Hien, P. T. Hung, J. Han, S. Lee, J. H. Lee, Y. W. Heo, Growth and gas sensing properties of methylammonium tin iodide thin film, Scr. Mater. 178 (2020) 108-113. http://doi.org/10.1016/j.scriptamat.2019.10.049.

[35] X. Li, T. Tan, W. Ji, W. Zhou, Y. Bao, X. Xia, Z. Zeng, Y. Gao, Remarkably Enhanced Methane Sensing Performance at Room Temperature via Constructing a Self-Assembled Mulberry-Like ZnO/SnO_2 Hierarchical Structure, Energy & Environmental Materials. 7 (2024) e12624. http://doi.org/10.1002/eem2.12624.

[36] Y. Dang, G. Tong, W. Song, Z. Liu, L. Qiu, Luis K. Ono and Y. Qi, Interface engineering strategies towards $Cs_2AgBiBr_6$ single-crystalline photodetectors with good Ohmic contact behaviours, J. Mater. Chem. C, 2020, 8, 276--284, https://doi.org/10.1039/c9tc04780h.

[37] Athira M, S. P. Bharath, S. Angappane, SnO_2-NiO heterojunction based self-powered UV photodetectors , Sens. Actuators A Physical 340 (2022) 113540, https://doi.org/10.1016/j.sna.2022.113540.

[38] Z. Zhang, Y. Liang, H. Huang, X. Liu, Q. Li, L. Chen, D. Xu, Stable and Highly Efficient Photocatalysis with Lead-Free Double-Perovskite of $Cs_2AgBiBr_6$, Angew. Chem. Int. Ed. Engl. 58 (2019) 7263-7267. http://doi.org/10.1002/anie.201900658.

[39] Xiao Luo, Yu Wang, Kevin Peter Homewood, Xuxing Chen and Yun Gao, Tandem $CdS/TiO_2(B)$ nanosheet photocatalysts for enhanced H_2 evolution, Appl. Surf. Sci., 515 (2020) 145970. http://doi.org/10.1016/j.apsusc.2020.145970.

[40] H. Wang, Y. Zou, H. Guo, W. Yu, X. Guo, X. Li, Z. Zhang, G. Liu, Sh. Yang, Zh. Tang, B. Qu, Zh. Chen, and L. Xiao, Passivating A-Site and X-Site Vacancies Simultaneously via N-Heterocyclic Amines for Efficient $Cs_2AgBiBr_6$ Solar Cells, ACS Appl. Mater. Interfaces 16 (2024) 4099−4107. https://doi.org/10.1021/acsami.3c11658.